Sliding charge-density-wave transport in micron-sized wires of $Rb_{0.30}MoO_3$

O. C. Mantel, C. A. W. Bal, C. Langezaal, C. Dekker, and H. S. J. van der Zant
Department of Applied Physics and DIMES, Delft University of Technology, Lorentzweg 1, 2628 CJ Delft, The Netherlands
(Received 26 March 1999)

We study sliding charge-density-wave (CDW) transport in mesoscopic wires of $Rb_{0.30}MoO_3$. The wires, with a width of 2 μm and contact spacings down to 1 μm, have been patterned into thin films by use of optical and electron-beam lithographic techniques. CDW sliding is evident from the nonlinear $I(V)$ characteristics below the Peierls temperature. The threshold field E_T for depinning of the CDW is 2–3 orders of magnitude higher than in bulk $Rb_{0.30}MoO_3$ crystals, and increases exponentially with decreasing temperature down to about 50 K. At lower temperatures, the shape of the $I(V)$ curves changes, and nonlinearity sets in at lower voltages. The observed transport properties are discussed in terms of CDW sliding and, at low temperatures, in terms of hopping of solitonlike excitations in the CDW lattice. [S0163-1829(99)16431-2]

I. INTRODUCTION

The sliding state of charge-density waves (CDW's) has been studied extensively in a variety of organic and inorganic materials.[1] CDW's that are incommensurate with the underlying lattice can slide if a moderate field, needed for depinning from impurities, is applied. CDW sliding gives rise to several unusual phenomena such as narrow-band noise, mode locking on applied ac frequencies, and hysteresis effects.

Many bulk properties of CDW's can be qualitatively understood within the Fukuyama-Lee-Rice (FLR) model.[2] This model treats the CDW as an elastic medium that interacts with impurities by adjusting its phase. In most CDW conductors, the CDW phase is weakly pinned, which means that the phase is only partly adjusted at the impurities. In this case, the phase-coherence length can be of the order of micrometers along the chains.[3] Studies of CDW transport have up till now mainly been performed on bulk samples, which consist of many phase-coherent domains.

Recently, CDW transport on mesoscopic length scales has received considerable attention, both theoretically and experimentally. For instance, Bogacheck *et al.*[4] predicted a periodic Aharonov-Bohm-like oscillation of the electrical conductance as a function of magnetic flux. Such an oscillation was indeed found for a $NbSe_3$ crystal, in which 15-nm-wide columnar defects were created by irradiation with 250-MeV Xe ions.[5] The precise mechanism behind this oscillation has not yet been clarified.[6] The electrical transport through heterostructures of CDW material with normal metals and superconductors is another aspect of mesoscopic CDW physics. Such systems have to date only been studied theoretically.[7–9] For instance, it has been predicted[7] that dissipationless currents can flow through the normal metal region N in a CDW-N-CDW junction.

We have developed techniques to enable transport measurements of CDW's in the mesoscopic regime. Earlier, we reported the growth of thin films of the blue bronze $Rb_{0.30}MoO_3$.[10] The blue bronzes $A_{0.30}MoO_3$ (A=K, Rb, Tl) are among the most extensively studied inorganic CDW conductors. Their strongly anisotropic crystal structure consists of slabs of weakly linked chains of MoO_6 octahedra that are separated by the alkali ions. Below a Peierls temperature of 182 K, the Fermi surface is completely gapped. Sliding CDW transport can then occur along the chains of MoO_6 octahedra, i.e., parallel to the crystallographic b axis. The thin films are patterned by use of electron-beam lithographic and photolithographic techniques.[11] In this way, wire structures of micrometer dimensions can be defined.

Here we present electrical transport measurements on such lithographically fabricated wires. After a description of the sample fabrication process and the experimental aspects (Secs. II and III), we will present the results of electrical transport measurements in Sec. IV. The data show clear evidence of sliding of CDW's below 180 K. In the discussion (Sec. V), we will focus on the pinning behavior and on the electrical transport at low temperatures.

II. SAMPLE FABRICATION

Wire structures are patterned into $Rb_{0.30}MoO_3$ films with a thickness of 0.3 μm. The films are grown on 5 $\times$5-mm^2 $Al_2O_3(012)$ substrates by use of pulsed-laser deposition at a typical temperature of 440 °C.[10] They consist of micrometer-sized grains that have CDW-conducting chains parallel to the substrate plane. Within this plane, however, the chains are randomly oriented. The patterning process was discussed in detail in Ref. 11. Here we restrict ourselves to a short description with the relevant process parameters.

Patterning of the blue bronze wires is carried out by optical lithography. First a 200-nm-thick layer of Au is evaporated to protect the film from water-based solutions. Then a 1.1-μm-thick layer of SR1813 photoresist is spun onto the sample, and baked at 90 °C during 30 min. Exposure of the resist is done through a glass mask by use of a Karl Susz aligner. The resist is developed in a water-based developer for 1 min. Argon-ion milling of Au and $Rb_{0.30}MoO_3$ is then performed in a Kaufmann source. The typical etch rate for blue bronze is 350 nm/h. After etching, the remains of Au are removed by dipping the sample for a few seconds in a water-based KI/I_2 solution. Remnants of resist are dissolved in boiling acetone.

Definition of gold contacts is done by both optical and electron-beam lithographic techniques. In the case of optical lithography, a sandwich of 15-nm Cu and 200-nm Au is

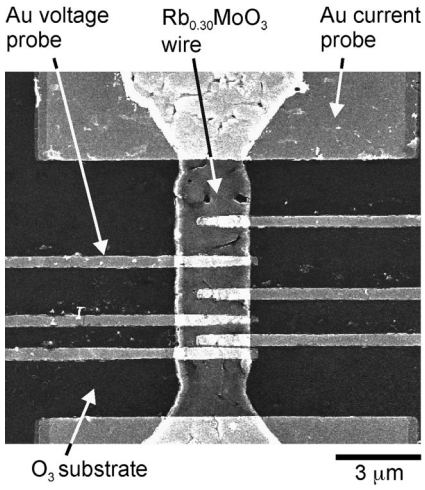

FIG. 1. SEM image of a wire structure patterned into a 0.3-μm thin film of $Rb_{0.30}MoO_3$. Gold current pads and 400-nm-wide voltage probes have been defined on top of the wire by *e*-beam lithography. Distances between middles of the voltage probes, from top to bottom, are 1.5, 1.25, 1.0, 0.75, and 0.5 μm.

evaporated. The Cu interface layer serves to improve the adhesion between wire and contact. Then a resist pattern is defined in a process similar to that used for the definition of the wires. Ar-ion milling of the Cu/Au sandwich typically takes 10 min. By using this process, contact spacings down to 2 μm have been realized.

Smaller contact spacings are obtained by electron-beam lithography. In this case, a lift-off process is used. A double layer of *PMMA*/*MMA* electron-beam resist is spin coated on top of the $Rb_{0.30}MoO_3$ wires. To avoid charging of the insulating Al_2O_3 substrate during electron-beam exposure, a 20-nm coating of Au is then sputtered. Exposure is performed by use of an electron-beam pattern generator (Leica HR5, 100 kV), and the exposed resist is developed in a mixture of methyl-isobutyl ketone and 2-propanol. Prior to evaporation of the metal contacts, the remains of the Au coating are removed by 30 s of Ar-ion milling. In order to obtain sufficient step coverage across the edge of the wire, different evaporation angles are used. Typical thicknesses are 10 nm of Ti (which serves as an adhesion layer) and 60 nm of Au. Lift-off is achieved by dissolving the resist in boiling acetone.

Figure 1 shows a top-view scanning electron microscope (SEM) image of a wire structure. Contacts have been defined by electron-beam lithography. The wire has a width of 2.6 μm and a length between current pads of 10 μm. Within the wire, the granular structure of the blue bronze film is visible. At the ends of the wire, current can be injected. To reduce the contact resistance of the current pads, a large overlap area has been chosen. Six Au strips with spacings down to 100 nm connect to the wire as voltage probes. Tilted-SEM images at higher magnifications confirm that step coverage of these voltage probes is obtained at the edges of the wire. The structure is electrically connected by ultrasonic wire bonding to 150×150-μm^2 Au contact pads outside the image of Fig. 1.

III. EXPERIMENTAL ASPECTS

Current-voltage characteristics have been measured in a helium-flow cryostat by current biasing and determining the resulting voltage across two voltage probes. The measurements reported in Sec. IV are all four-terminal measurements. In the normal configuration, current is injected at the large current pads at the ends of the wire, and voltage is measured with small probes near the middle. We have also used transposed four-terminal measurements. In this case, the current and voltage probes are interchanged, i.e., current is injected at the small probes and voltage is measured at the ends of the wire.

The contact resistance of a pair of voltage probes is obtained from subtracting its two- and four-terminal resistances. Independent measurements of single contacts are also obtained from three-terminal measurements. In this case, we use three adjacent contacts *A*, *B*, and *C*. The resistance of the middle contact *B* is determined by applying current between *A* and *B*, and measuring the resulting voltage between *B* and *C*. For small bias currents (typically 1 μA), contact resistances of the voltage probes range from 0.1 to 10 kΩ at room temperature, and from 10 to 1000 kΩ at 70 K. Assuming that the contact resistance scales with the overlap area between wire and metal pad, the contact resistance of the current pads is two orders of magnitude lower. The contact resistances of the voltage probes are high enough to exclude the possibility of significant current shunting in the normal configuration.

Several authors have used the difference between normal and transposed measurements to determine the phase-slip voltage needed for current conversion near the contacts.[12–15] Such a phase-slip analysis is not possible for our wires, because the resistance of the small contacts near the middle of the wire is strongly current dependent. If a typical current of 10 μA at 70 K is applied, the contact resistance decreases by a factor of 10 as compared to its low-bias value. This nonlinear contact resistance causes a difference between transposed and normal $I(V)$ curve,[16] which exceeds expected phase-slip voltages. For this reason, we have refrained from studying phase-slip phenomena for our blue bronze wires.

Experimentally, the small wire structures are more difficult to handle than bulk crystals. In particular the smallest voltage contacts, fabricated by *e*-beam lithography, can be easily damaged if they are used for current injection (transposed configuration). The blue bronze wires themselves can also be quite fragile; grains can be removed for high applied currents. Heating effects have been observed for high currents in the transposed configuration, when considerable power is dissipated at the small contacts. We only present those data for which heating effects are absent.

IV. ELECTRICAL TRANSPORT MEASUREMENTS

The room-temperature resistivity is measured to select those wires for which the grains have their CDW *b* axis aligned with the wire. For such grains, a resistivity of about 1 mΩ cm is expected.[17] For grains with the CDW axis perpendicular to the wire (but still in plane), the resistivity is a factor 20–80 higher. Measured resistivities of our wires vary from 0.7–500 mΩ cm, in reasonable agreement with these values. The values above 100 mΩ cm indicate that grain boundaries can also be important. Here we present only the measurements on wires with resistivities of 5 mΩ cm and

TABLE I. Contact spacing, room-temperature resistivity ρ(295 K), and threshold field E_T at 70 K for eight $Rb_{0.30}MoO_3$ wires. All wires are 2 μm wide and 0.3 μm thick. T^* denotes the temperature for which the resistivity is a factor 2 lower than expected from the BCS fit (see text).

Wire no.	Spacing (μm)	ρ (295 K) (mΩ cm)	E_T (70 K) (V/cm)	$T^*(K)$
1	10	3.2	160	
2	5	1.4	120	
3	5	1.2	120	48
4	3	1.3	130	
5	1.5	2.8	7	
6	1.25	3.6	22	46
7	1.25	0.7	27	48
8	1	3.5	290	43

lower. Only a few percent of the fabricated wires meet this criterion.

Low-resistivity wires display transport properties different from wires with higher resistivities, viz., a larger Peierls gap, and more pronounced nonlinear $I(V)$ characteristics with lower CDW depinning fields. In Table I, electrical transport properties are listed for eight such wires. We first describe the properties of the wires at small currents (Sec. IV A). In Sec. IV B we concentrate on the nonlinear $I(V)$ characteristics.

A. Low-bias transport

The low-bias resistivity is measured as a function of temperature T by using standard lock-in methods. Below about 30 K, sample resistances are too high for the use of such ac techniques. Here, the resistivity is determined from $I(V)$ curves that are recorded by sweeping the current at 1 mHz.

Figure 2 shows the resistance of wire 5 versus $1/T$ in the temperature interval 60–295 K. Upon decreasing temperature, the resistance first decreases. Below about 180 K, the resistance sharply increases, consistent with the opening of an energy gap at the Peierls transition temperature T_P. At 60 K, the resistance has increased by three orders of magnitude as compared to the room-temperature value. In the inset of Fig. 2, the resistivity of the same wire is plotted versus temperature. At room temperature, $\rho = 2.8$ mΩ cm. Above 225 K, the resistivity is proportional to the temperature, which is similar to the behavior of conventional metals in this temperature range. From a linear fit to the data, we find a temperature coefficient of 10 $\mu\Omega$ cm/K. For bulk blue bronze crystals, positive temperature coefficients of 8 $\mu\Omega$ cm/K (Ref. 18) and 2.5 $\mu\Omega$ cm/K (Ref. 19) along b have been reported. Three other wires show a similar positive temperature coefficient for $T > 225$ K, albeit with a smaller slope. For wires 1, 4, and 8, a slight increase of the resistivity with decreasing temperature is observed.

A broadening of the Peierls transition is observed for all wires. In Fig. 3, we plot $d\ln(\rho)/d(1/T)$ versus temperature for two wire structures, as well as for a bulk $Rb_{0.30}MoO_3$ crystal that serves as a reference (dotted line). The solid line denotes the resistivity for wire 3. Instead of a sharp peak at 182 K, a more gradual transition occurs at a somewhat lower temperature. Taking the temperature for which $d\ln(\rho)/d(1/T)$ has its maximum as the definition of the transition temperature, we find $T_P = 175$ K. An even stronger broadening of the Peierls transition is observed for most other wires. For example, the dashed line, denoting the resistivity for the wire of Fig. 2, shows no pronounced maximum in $d\ln(\rho)/d(1/T)$.

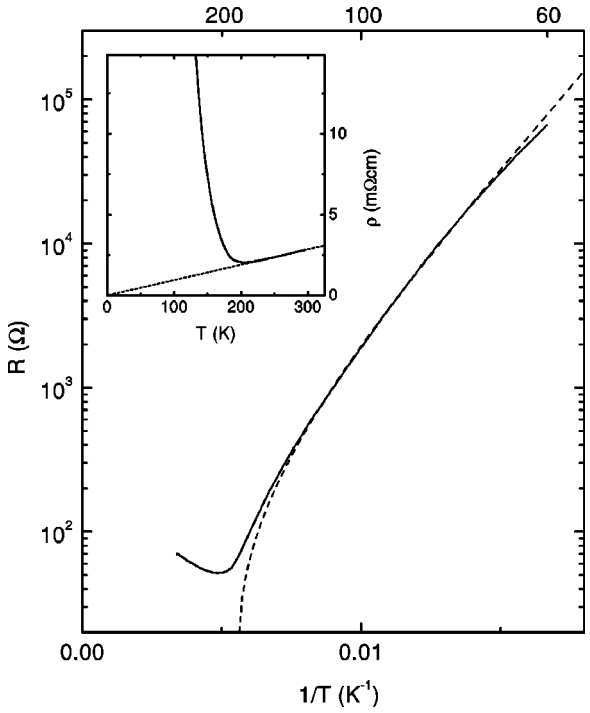

FIG. 2. Resistance vs inverse temperature for wire 5. In the temperature interval 70–160 K, the data have been fitted with $R \propto e^{\Delta(T)/k_BT}$ (dashed line), where $\Delta(T)$ has the BCS temperature dependence with fit parameter $\Delta(0)/k_B = 510$ K. The inset shows the resistivity on a linear scale. A linear fit for $T > 250$ K yields a positive temperature coefficient of 10 $\mu\Omega$ cm/K.

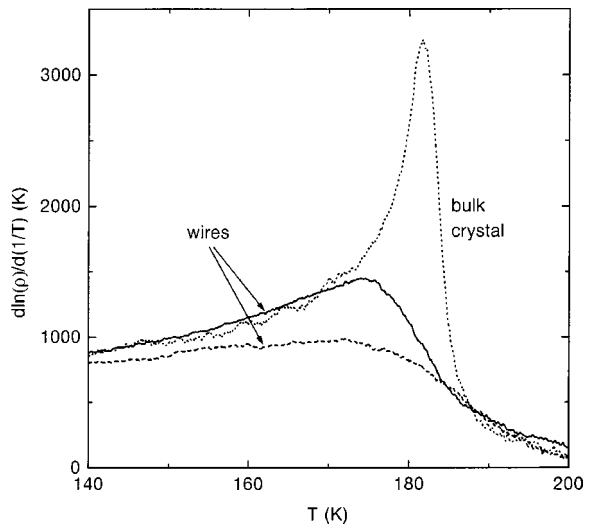

FIG. 3. $d\ln(\rho)/d(1/T)$ vs temperature, demonstrating the Peierls transition for wire 3 (solid line), wire 5 (dashed line), and for a 0.2-mm thick $Rb_{0.30}MoO_3$ crystal with voltage probes 1 mm apart (dotted line). For the wires, a broadening of the transition is observed at a somewhat lower temperature.

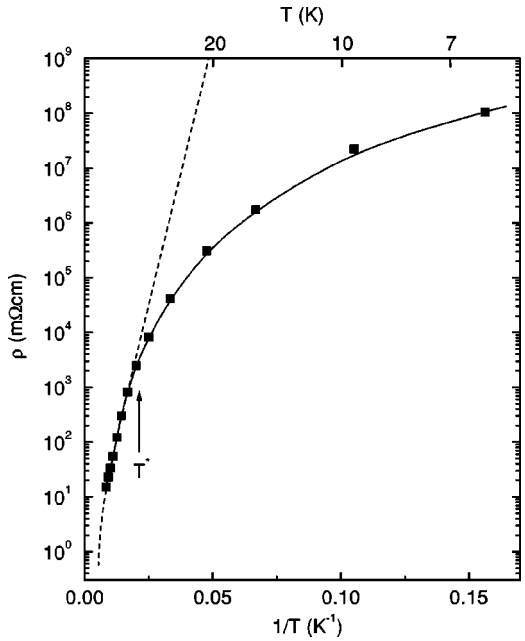

FIG. 4. Low-bias resistivity vs inverse temperature at temperatures below 120 K. The solid squares denote resistivities for wire 6; the solid curve is a guide to the eye. In the temperature range 70–120 K, the data have been fitted with a BCS temperature-dependent gap (dashed curve), similar to the method demonstrated in Fig. 2. Below 50 K, such a fit does not hold, i.e., the measured resistivities are lower than expected if thermally excited quasiparticles would be solely responsible for transport. T^* denotes the temperature for which the difference in resistivity between data and fit is a factor 2.

In the temperature region 70–160 K, the resistivity can be fitted with an exponential temperature dependence $R \propto e^{\Delta(T)/k_BT}$ (cf. the dashed line in Fig. 2), where $\Delta(T)$ is the energy gap with a temperature dependence calculated from BCS theory. For the wire of Fig. 2, we find $\Delta(0)/k_B = 510$ K. Other low-resistivity wires yield similar values, ranging from 460 to 510 K. The observed gap values agree well with the typical values of 350–500 K for bulk blue bronze that are reported in the literature.[19–21]

At very low temperatures, $R(T)$ does not a follow the BCS-like $e^{\Delta(T)/k_BT}$ dependence any longer, as illustrated in Fig. 4. The dashed line is the BCS dependence fitted to the data in the interval 70–160 K. The data deviate from this dependence below 50 K. We define T^* as the temperature for which the resistivity is a factor 2 lower than the value from the BCS fit. For the wire of Fig. 4, this yields $T^* = 47$ K. A similar flattening of the $\rho(1/T)$ dependence is found for the other wires, with T^* values in the small range of 43–48 K (Table I). The data suggest that below this temperature a mechanism different from thermal excitation of quasiparticles is responsible for the low-bias charge transport.

B. Sliding CDW transport

Sliding of charge-density waves is evident below 180 K from the nonlinear current-voltage characteristics. We have measured $I(V)$ curves by slowly (typically at 1 mHz) sweeping the current and recording the resulting voltage over the sample. Simultaneously, dV/dI is obtained from a small ac signal added to the dc sweep. The amplitude of this ac signal is 2.5 % of the full dc sweep amplitude. Below 30 K, high sample resistances prevent the use of ac techniques, and dV/dI is derived numerically from $I(V)$.

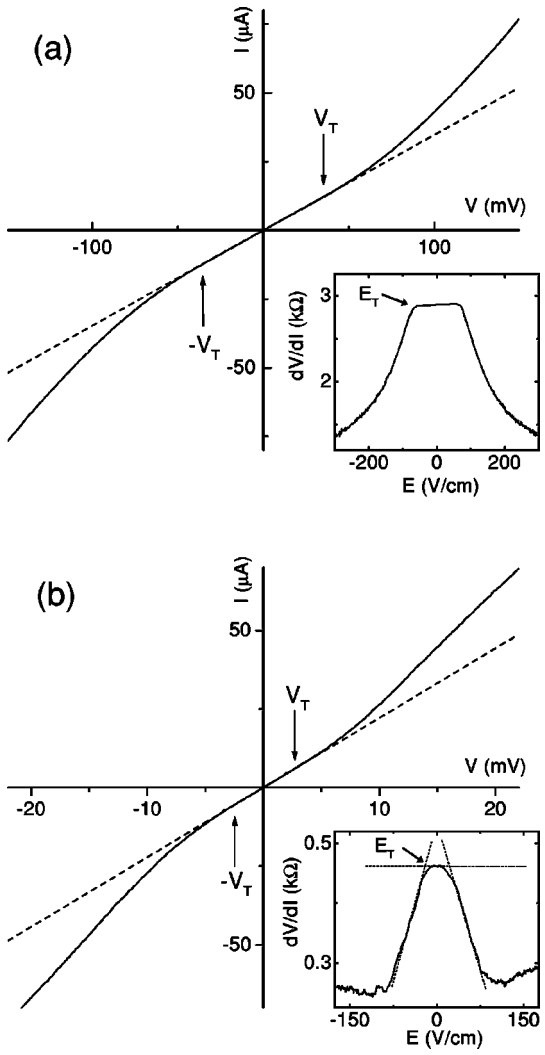

FIG. 5. $I(V)$ characteristics at 110 K for wire 3 (a) and wire 6 (b). Near the threshold voltage V_T, the $I(V)$ curves become nonlinear, consistent with the onset of sliding CDW transport. The insets show the corresponding differential resistances, and the procedure for determining E_T.

Typical $I(V)$ curves for two wires are shown in Fig. 5. For low-bias voltages, the $I(V)$ curves are linear (dashed line). A transition to a nonlinear region sets in near a threshold voltage V_T, consistent with the onset of CDW sliding. The value of V_T is determined from the corresponding dV/dI characteristics (see insets). For several wires, dV/dI is constant at low bias, and then sharply decreases at V_T. Such a behavior is demonstrated in the inset of Fig. 5(a). The threshold field E_T for depinning is 70 V/cm for this wire. Other wires show a more gradual nonlinearity [Fig. 5(b)]. For such wires, we define V_T by plotting the two tangents to the steepest part of the dV/dI, and determining the intersection points with the horizontal line through $dV/dI(0)$ [cf. the dashed lines in the inset of Fig. 5(b)]. For the data of Fig. 5(b), we find $V_T = 2.7$ mV, corresponding to a threshold field of 22 V/cm.

Measured values for E_T at 70 K are listed in Table I. They vary strongly from wire to wire, and range from 5 to 300 V/cm. These typical E_T values are 1–2 orders of magnitude larger than values reported on thin crystals with comparable thicknesses of 0.1–2 μm.[22] The lowest threshold fields are found for wires that show a gradual transition to the sliding state, i.e., for wires 2, 5, 6, and 7. For the other wires, with a sharp onset of sliding, E_T is larger than 100 V/cm (wires 1, 3, 4, and 8).

Figure 6(a) shows various dV/dI characteristics measured at temperatures in the range 50–200 K. For temperatures up to 170 K, a sharp onset of nonlinear conduction is observed. The shape of dV/dI versus V remains qualitatively the same, but E_T decreases when temperature is increased. At higher temperatures, a clear threshold field can no longer be defined. The nonlinearity disappears, in agreement with the breakdown of the CDW state near 180 K. Figure 6(b) shows E_T versus T. Between 60 and 180 K, the data can be fitted by $E_T = E_T(0)e^{-T/T_0}$, with $T_0 = 77$ K. Similar fits could be performed for all wires that show a sharp threshold field for depinning. Values for T_0 range from 70 to 200 K. Note that the temperature dependence of E_T for our wires is radically different from earlier observations in bulk crystals.[23–26] The temperature dependence for blue bronze crystals has not yet fully been elucidated, and seems to depend on crystal quality. Between 50 and 100 K, however, all previous authors have reported an increase of E_T with increasing temperature, contrary to our wires.

Below 50 K, we observe a change of the nonlinear behavior. Figure 7 shows the $I(V)$ characteristics for wire 3 at several temperatures between 15 and 50 K. Instead of the sharp threshold voltage observed in Fig. 5(a), a smooth onset of nonlinearity is observed. Furthermore, the field at which nonlinearity sets in *increases* with increasing temperature. We determine E_T by numerically differentiating the curves of Fig. 7, and then plotting three tangents to the resulting dV/dI [as illustrated in Fig. 5(b)]. In the inset of Fig. 7, the corresponding values of E_T are plotted versus temperature. The data can be fitted with a linear temperature dependence $E_T = \gamma T$, which yields a slope $\gamma = 2.7 \pm 0.2$ V/cmK. A similar decrease of E_T with decreasing temperature is found for other wires.

The sliding-CDW state is accompanied by high-amplitude broadband noise (BBN). Figure 8 shows the root-mean-square noise voltage V_{rms} in the frequency window 0.1–100 Hz, measured at several temperatures. The asterisks denote the sliding threshold V_T, as determined from the dV/dI characteristics. The noise curves generally show a maximum at a certain electric field, followed by a gradual decrease of V_{rms} at larger bias. At 35 K, the maximum of the noise level occurs at a bias voltage larger than V_T. At 50 and 70 K, the maximum is found at a voltage *smaller* than V_T. Also at the higher temperatures of 90 and 110 K, an increase of the noise level is observed below V_T, but the effect is less pronounced, and the noise level remains more or less constant at higher bias. By analyzing the frequency spectrum (not shown), we find that for all temperatures the noise power spectral density is proportional to $f^{-\alpha}$, with α varying between 0.8 and 1.6.

The noise data of Fig. 8 show a strong hysteretic behavior. Especially at low temperatures, the shape of the noise curve depends on the sweep direction of the current (indicated by the arrows in Fig. 8). Coming from high bias, V_{rms} drops sharply to the noise floor of the setup near V_T. For a positive sweep direction, however, a more gradual change of the noise is observed at a lower bias voltage.

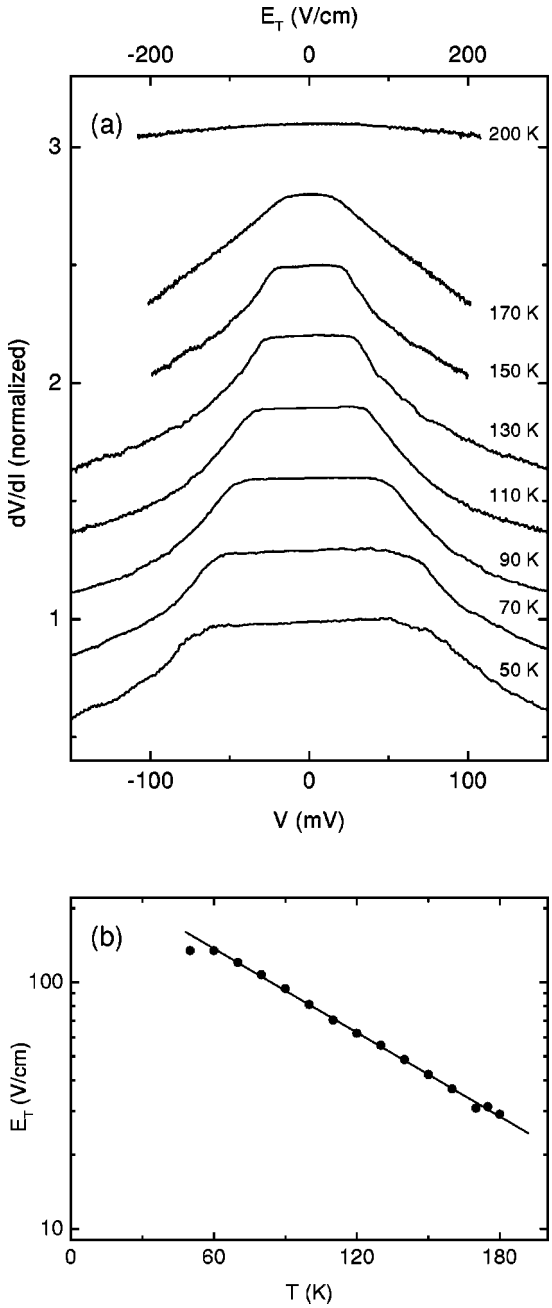

FIG. 6. Dependence of the threshold field on temperature for wire 3. (a) dV/dI vs V for several temperatures, normalized to its value at $V = 0$. Subsequent curves have been offset by 0.3. (b) The threshold field E_T for sliding, as determined from the curves in (a). E_T increases with decreasing temperature down to 60 K. The solid line shows a fit to the data of $E_T = E_T(0)e^{-T/T_0}$, yielding $T_0 = 77$ K and $E_T(0) = 300$ V/cm.

V. DISCUSSION

The selected wires, with room-temperature resistivities of less than 5 mΩ cm, show clear signatures of sliding-CDW

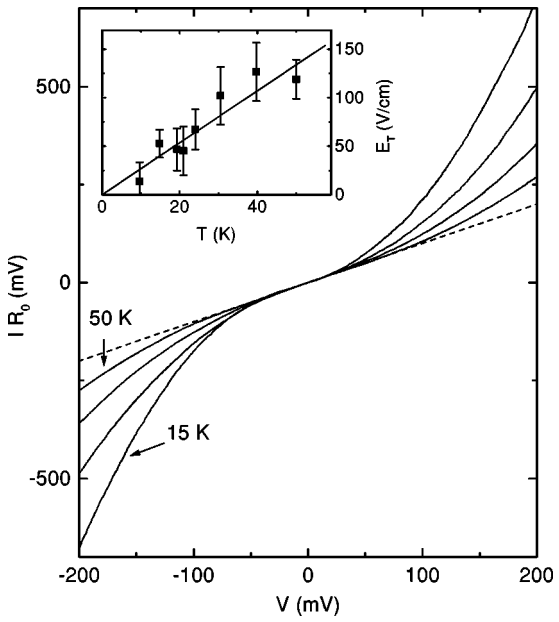

FIG. 7. $I(V)$ curves at 15, 19, 24, and 50 K, for wire 3. The current has been multiplied by the low-bias resistance R_0, allowing for a comparison between curves at different temperatures. Around $V=0$, all curves thus have slope 1 by definition (dashed line). Upon increasing voltage, nonlinearity sets in gradually. The inset shows the temperature dependence of the threshold field E_T. From a weighted linear fit to the data we find $E_T=2.68\,T$(V/cm).

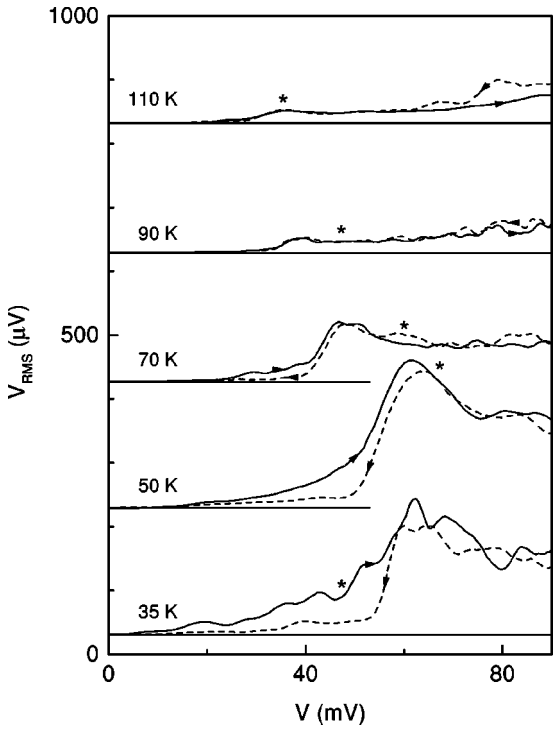

FIG. 8. Root-mean-square noise voltage V_{rms} in the frequency window 0.1–100 Hz as a function of bias voltage (wire 3). Curves for subsequent temperatures are offset by 200 μV for clarity; the sweep direction is indicated by arrows. The asterisks denote the threshold voltage V_T for sliding, as determined from the $I(V)$ characteristics. A strong increase of the noise voltage is observed near V_T.

transport. Several aspects of the properties of the wires, however, are different from those of bulk crystals. The threshold field for sliding is 2–3 orders of magnitude larger, and shows an exponential *decrease* with temperature instead of an increase. The Peierls transition is broadened, and the transition temperature is reduced. All these trends are consistent with measurements on very thin crystals of TaS_3.[27,28] An increase of E_T for thin crystals has as well been measured in $NbSe_3$ (Ref. 29) and $Rb_{0.30}MoO_3$.[26] The similarity of our data to measurements on very thin crystals indicates that size effects play a role in our wires.

Several pinning mechanisms may be responsible for the high threshold fields observed for our wires. First surface pinning must be considered. Our wires have typical cross sections of only 1 μm^2, and they have a large surface roughness due to the granular nature of the films. Therefore, we believe that the surface contributes to the CDW pinning. In the bulk of the wires, the CDW may be pinned by grain boundaries, or by impurities in the $Rb_{0.30}MoO_3$ lattice. Since the typical grain size for our wires is of the order of 1 μm, one or a few grain boundaries can be present between the voltage probes. Impurities may be dislocations, substitutional defects, or other lattice defects within the $Rb_{0.30}MoO_3$ grains.

The interaction between CDW and bulk impurities is described by the FLR model.[2] This model treats the CDW as an elastic medium that interacts with impurities by locally adjusting its phase. Depending on the strength and concentration of the pinning centers, two regimes can be distinguished. In the strong-pinning regime, the phase is fully adjusted at every pinning center. In the weak-pinning regime, however, the elastic energy of the CDW dominates, and the phase is only partly adjusted near impurities. In one dimension, the ratio ϵ_{FLR} of the pinning energy U_{pin} of an impurity and the average elastic energy U_{elast} of the CDW, needed for deformation at the impurity, can be written as

$$\epsilon_{FLR}=\frac{U_{pin}}{U_{elast}}=\frac{4U_{pin}}{\pi\hbar v_F n_{imp}}, \tag{1}$$

where v_F is the Fermi velocity, and n_{imp} is the impurity concentration. For strong pinning, $\epsilon_{FLR}\gg 1$, whereas weak pinning occurs for $\epsilon_{FLR}\ll 1$. In the latter case, the phase-coherence length can be much larger than the impurity-impurity distance.

We can use the temperature dependence of the threshold field (Fig. 6) to determine ϵ_{FLR}, since k_BT_0 is a measure for the typical pinning energy U_{pin},[30] and $E_T(0)$ yields a value for the impurity concentration. At zero temperature, the threshold field is the field for which the energy loss eE_TL_0, due to motion in the electric field between two impurities with spacing L_0, equals U_{pin}. Thus

$$L_0=\frac{U_{pin}}{eE_T(0)}. \tag{2}$$

For wire 3 with $E_T(0)=300$ V/cm and $T_0=77$ K, we find $L_0=220$ nm. This distance is smaller than the typical grain size of 1 μm for the wires, suggesting that grain boundary pinning is not the dominant pinning mechanism. Given this average impurity spacing, there are about 20 impurities along a distance of 5 μm between the voltage probes. Using v_F

$=2\times10^5$ m/s (Ref. 31) and $k_BT_0=U_{pin}$, we find, with Eq. (1), that $\epsilon_{FLR}=14$. A similar analysis can be performed for other wires. We always find $\epsilon_{FLR}\gg1$, indicating that the CDW's for our wires are strongly pinned.

A remarkable change of both the linear and the nonlinear properties of our $Rb_{0.30}MoO_3$ wires occurs below 50 K. The low-bias resistivity at low temperatures is different from the activated behavior that would be measured if excited quasiparticles were the responsible transport mechanism. At the same time, the dependence of E_T on temperature changes to a linear increase with increasing temperature. These trends are in qualitative agreement with measurements on TaS_3 crystals at low temperatures.[32] They indicate that at low temperatures a transport mechanism other than CDW sliding or excitation of quasiparticles is dominant.

The behavior of the low-bias resistivity (Fig. 4) below 50 K may be explained by the existence of solitonlike excitations in our wires.[32] In CDW materials, such solitons are charged phase deformations of the CDW, which can move in an electric field. The excitation energy for a soliton is expected to be smaller than the CDW gap, and to be of the order of k_BT_P.[33] At low temperatures, the contribution of thermally excited quasiparticles to the low-bias conductivity freezes out, and solitons become the dominant charge carriers.

The motion of charged solitons in CDW systems seems to resemble the hopping conductivity mechanism in disordered conductors. Previous authors[32,34] have shown that below 100 K the temperature dependence of the resistivity of TaS_3 can be fitted with Mott's equation for variable-range hopping (VRH),[35]

$$ln(\sigma)\propto-\left(\frac{T_s}{T}\right)^{\gamma}, \tag{3}$$

where T_s is a characteristic temperature, and $\gamma=(1+d)^{-1}$ depends on the dimensionality d of the system. In TaS_3, the best fits are obtained with $d=1$. Our low-temperature data are consistent with Eq. (3). Due to the limited number of data points at low temperature, however, the dimensionality d cannot be unambiguously determined for our wires.

The gradual nonlinearity of the $I(V)$ curves for temperatures below 50 K can be explained with the VRH model. Apsley and Hughes[36] calculated the electric-field dependence of hopping conduction in disordered systems. They found that $I(V)$ characteristics are nonlinear, with a decrease of the resistivity with increasing applied electric field. The typical electric field for the onset of nonlinear conduction depends linearly on temperature,

$$E_T=\frac{0.2k_B}{el}T, \tag{4}$$

where l is a length which can be interpreted as the typical distance between impurities. Using the fit of the inset of Fig. 7, we find $E_T=268\ T$, resulting in $l=64$ nm. Note that this impurity spacing is of the same order of magnitude as the impurity spacing found from the pinning analysis. Analysis for other wires results in similar impurity spacings.

A second threshold field, which marks the onset of sliding conduction, may occur at higher applied electric fields in the low-temperature regime. This suggestion is supported by the strong increase of the BBN voltage for high applied fields well above E_T (cf. the curve for 35 K in Fig. 8). Such a second threshold field has also been found in the $I(V)$ characteristics of thin TaS_3 crystals.[32]

VI. CONCLUSION

The thin-film technology for $Rb_{0.30}MoO_3$ allows the fabrication of micron-sized wires with a well-defined short length. We have shown that sliding-CDW transport occurs in such wires below the transition temperature of about 180 K. The threshold field E_T for depinning is 1–2 orders of magnitude higher than for thin $Rb_{0.30}MoO_3$ crystals, and decreases exponentially with increasing temperature. An analysis in terms of the FLR model for CDW depinning shows that the CDW's in our wires are strongly pinned. At low temperatures, the electrical transport properties change. This change is consistent with a transition to hopping of solitonlike phase deformations as the dominant electrical transport mechanism.

ACKNOWLEDGMENTS

We wish to acknowledge Mark Visscher for useful discussions. This work was supported by the Netherlands Foundation for Fundamental Research on Matter (FOM). H.S.J.v.d.Z. was supported by the Dutch Royal Academy of Arts and Sciences (KNAW).

[1] For reviews, see *Electronic Properties of Inorganic Quasi-One-Dimensional Compounds*, edited by P. Monceau (Reidel, Dordrecht, 1985),Pts. I and II; G. Grüner, *Density Waves in Solids* (Addison-Wesley, Reading, MA, 1994).
[2] H. Fukuyama and P. A. Lee, Phys. Rev. B **17**, 535 (1978); P. A. Lee and T. M. Rice, *ibid.* **19**, 3970 (1979).
[3] S. M. DeLand, G. Mozurkewich, and L. D. Chapman, Phys. Rev. Lett. **66**, 2026 (1991).
[4] E. N. Bogachek, I. V. Krive, I. O. Kulik, and A. S. Rozhavsky, Phys. Rev. B **42**, 7614 (1990).
[5] Yu. I. Latyshev, O. Laborde, P. Monceau, and S. Klaumünzer, Phys. Rev. Lett. **78**, 919 (1997).
[6] M. I. Visscher and B. Rejaei, Europhys. Lett. **43**, 617 (1998).
[7] M. I. Visscher and G. E. W. Bauer, Phys. Rev. B **54**, 2798 (1996).
[8] B. Rejaei and G. E. W. Bauer, Phys. Rev. B **54**, 8487 (1996).
[9] M. I. Visscher and B. Rejaei, Phys. Rev. Lett. **79**, 4461 (1997).
[10] H. S. J. van der Zant, O. C. Mantel, C. Dekker, J. E. Mooij, and C. Træholt, Appl. Phys. Lett. **68**, 3823 (1996); O. C. Mantel, H. S. J. van der Zant, A. J. Steinfort, C. Dekker, C. Træholt, and H. W. Zandbergen, Phys. Rev. B **55**, 4817 (1997).
[11] O. C. Mantel, C. A. W. Bal, C. Langezaal, C. Dekker, and H. S. J. van der Zant, J. Appl. Phys. (to be published).
[12] J. C. Gill, Solid State Commun. **44**, 1041 (1982).
[13] J. C. Gill, Phys. Rev. Lett. **70**, 331 (1993).
[14] M. P. Maher, T. L. Adelman, D. A. DiCarlo, J. P. McCarten, and R. E. Thorne, Phys. Rev. B **52**, 13 850 (1995).

[15] O. C. Mantel, F. Chalin, C. Dekker, H. S. J. van der Zant, Yu. I. Latyshev, B. Pannetier, and P. Monceau, Synth. Met. (to be published).

[16] For high contact resistances, current is injected homogeneously over the full width of the probe. If we denote the spacing between voltage probes by d, and the width of a probe by w, voltage is in this case measured over a distance $d+w$. If, on the other hand, the contact resistance is negligibly small as compared to the wire resistance, current injection is inhomogeneous, and the distance over which voltage is measured decreases to d. Since for our wires w is comparable to d, inhomogeneous current injection results in a significant decrease of the measured resistance value.

[17] E. Bervas, Ph.D. thesis, Université Scientifique, Technologique et Médicale de Grenoble, 1984.

[18] R. Brusetti, B. K. Chakraverty, J. Devenyi, J. Dumas, J. Marcus, and C. Schlenker, in *Recent Developments on Condensed Matter Physics*, (Plenum, New York, 1981), Vol. 2, pp. 181–190.

[19] W. Brütting, P. H. Nguyen, W. Rieß, and G. Paasch, Phys. Rev. B **51**, 9533 (1995).

[20] L. F. Schneemeyer, F. J. DiSalvo, S. E. Spengler, and J. V. Waszczak, Phys. Rev. B **30**, 4297 (1984).

[21] C. Schlenker, J. Dumas, C. Escribe-Filippini, and H. Guyot, in *Low-Dimensional Electronic Properties of Molybdenum Bronzes and Oxides*, edited by C. Schlenker (Kluwer, Dordrecht, 1989), pp. 159–257.

[22] W. Xue-Mei, Z. Dian-lin, and Z. Yuheng, Phys. Rev. B **45**, 13 250 (1992).

[23] A. Maeda, T. Furuyama, and S. Tanaka, Solid State Commun. **55**, 951 (1985).

[24] R. M. Fleming, L. F. Schneemeyer, and D. E. Moncton, Phys. Rev. B **31**, 899 (1985); R. M. Fleming, R. J. Cava, L. F. Schneemeyer, E. A. Rietman, and R. G. Dunn, *ibid.* **33**, 5450 (1986).

[25] C. Schlenker and J. Dumas, Physica B **143**, 103 (1986).

[26] W. Xue-Mei and Z. Dian-Lin, Solid State Commun. **91**, 283 (1994).

[27] D. V. Borodin, F. Ya. Nad', Ya. S. Savitskaya, and S. V. Zaitsev-Zotov, Physica B **143**, 73 (1986).

[28] D. V. Borodin, S. V. Zaitsev-Zotov, and F. Ya. Nad', Zh. Éksp. Teor. Fiz. **93**, 1394 (1987) [Sov. Phys. JETP **66**, 793 (1987)].

[29] J. McCarten, M. Maher, T. L. Adelman, and R. E. Thorne, Phys. Rev. Lett. **63**, 2841 (1989).

[30] J. R. Tucker, W. G. Lyons, and G. Gammie, Phys. Rev. B **38**, 1148 (1988).

[31] J. P. Pouget, in *Low-Dimensional Electronic Properties of Molybdenum Bronzes and Oxides* (Ref. 21), pp. 87–157.

[32] M. E. Itkis, F. Ya. Nad', and P. Monceau, J. Phys.: Condens. Matter **2**, 8327 (1990).

[33] S. A. Brazovskii, Zh. Éksp. Teor. Fiz. **78**, 677 (1980) [Sov. Phys. JETP **51**, 342 (1980)].

[34] S. K. Zhilinskii, M. E. Itkis, I. Yu. Kalnova, F. Ya. Nad', and V. B. Preobrazhenskii, Zh. Éksp. Teor. Fiz. **85**, 362 (1983) [Sov. Phys. JETP **58**, 211 (1983)].

[35] N. F. Mott and E. A. Davis, *Electronic Processes in Non-Crystalline Materials*, 2nd ed. (Clarendon Press, Oxford, 1979).

[36] N. Apsley and H. P. Hughes, Philos. Mag. **30**, 963 (1974).